DOI: 10.61782/fa.2023.0136

forum acusticum 2023

A COMPUTATIONAL STUDY OF SOUND SCATTERING BY ELLIPTIC VORTICES

L. Martin-Martin[1*,2] **V. Clair**[1] **C. Bogey**[1] **G. Gabard**[3]

[1] Univ Lyon, CNRS, Ecole Centrale de Lyon, INSA Lyon, Univ Claude Bernard Lyon I, Laboratoire de Mécanique des Fluides et d'Acoustique, UMR 5509, 69130 Ecully, France

[2] Siemens Digital Industries Software, 92320 Châtillon, France

[3] LAUM, Le Mans Université, Avenue Olivier Messiaen, 72085 Le Mans, France

ABSTRACT

The scattering of acoustic waves by elliptic vortices is studied in two dimensions by solving the Linearized Euler Equations with the Discontinuous Galerkin Method. The parameters of interest for this work are: the aspect ratio of the elliptic vortex, the orientation of the vortex with regard to the incident acoustic waves, the magnitude of the vortex velocity and the ratio between the acoustic wavelength and the size of the vortex λ_0/r_0. The vortex orientation and its velocity magnitude affect the number of visible interference patterns, their amplitude and their angular spread around the vortex. The parameter λ_0/r_0 also has an effect on the width of individual interference beams. The aspect ratio of the vortex has a milder effect on the scattered field. Next, the scattering observed when the vortex is convected by a uniform mean flow is studied. During the convection of the vortex, the scattered field evolves because the orientation of the incident wavefronts and the ratio λ_0/r_0 vary with the position of the vortex. The signals recorded at several microphone positions show that the scattering of the acoustic field leads to a spectral broadening associated with the convection of the vortex.

Keywords: *Acoustic scattering, Elliptic vortex, Discontinuous Galerkin method, Linearized Euler Equations*

**Corresponding author*: *laura.martin@ec-lyon.fr.*

***Copyright**: ©2023 L. Martin-Martin This is an open-access article distributed under the terms of the Creative Commons Attribution 3.0 Unported License, which permits unrestricted use, distribution, and reproduction in any medium, provided the original author and source are credited.*

1. INTRODUCTION

When acoustic waves propagate through a volume of turbulence such as a jet shear layer, the propagation is affected by the disturbances in the medium properties, leading to spatial scattering. If the volume of turbulence is convected, the sound scattered by the inhomogeneities is affected by a Doppler effect, which leads to a spectral broadening [1]. In many instances, the resulting acoustic spectra consists in a peak at the source frequency, with a reduced amplitude, and sidelobes around the peak associated with the scattered field. The unsteady modelling of a turbulent mixing layer is complex. It can be achieved numerically, for example through Direct Numerical Simulation, but at a high computational cost. Alternatives exist, such as Large Eddy Simulation [2] where only the large turbulent scales are resolved, or stochastic methods such as RPM [3] where a turbulent field is reproduced from its statistical properties. In previous work [1, 2], it was shown that the scattering was mostly due to the contribution of the largest most energetic eddies of the shear layer. Thus, some general properties of the spectral broadening can be understood by considering only the most energetic eddies instead of all the turbulent scales [4]. If these eddies are arranged so that the interaction between their scattered acoustic field and other eddies can be neglected, the scattering by a single eddy can be studied and the observations can be generalized to complete shear layers. Previous studies on the acoustic scattering by a single vortex in the literature consider a round vortex as the turbulent structure, although, in mixing layers, the eddies are slightly elongated in the axial direction [5]. This motivated the present work on the acoustic scattering by an elliptic vortex. The Kirchhoff vortex model was selected

as it can be defined analytically in a parametric way, and it satisfies the Euler equations [6]. The effects of several parameters are assessed such as the aspect ratio and the orientation of the vortex which differentiate the elliptic vortex from the circular vortex. The influence of the velocity magnitude of the vortex and of the ratio between the acoustic wavelength and the vortex size is also studied.

This article is structured as follows. The definition of the Kirchhoff vortex and its parameters are presented in section 2. The configuration used in the numerical simulations is described in section 3. In section 4, the study of the different parameters defining an elliptic vortex is presented. The effects of the convection of the vortex by a uniform mean flow in the spatial and frequency domains are studied in section 5.

2. VORTEX DEFINITION

The vortex chosen for this study is defined by Kirchhoff [6] depicted in Fig. 1. The shape of the vortex depends on its semi-major axis $a = r_0(1+\epsilon)$ and its semi-minor axis $b = r_0(1-\epsilon)$, where ϵ controls the degree of ellipticity and r_0 is the equivalent radius of a circular vortex if $\epsilon = 0$. The aspect ratio of the vortex is defined by a/b. The orientation of the major axis is given by the parameter θ, which is the angle between the direction of propagation of the incident wave at the center of the vortex $(0,0)$ and the direction of the major axis. The core of the vortex is the region D_θ where the vorticity Ω is uniform, defined as

$$D_\theta = \{(x,y) = (r\cos(\zeta), r\sin(\zeta)) \mid [r\cos(\zeta-\theta-\pi/4)/a]^2 + [r\sin(\zeta-\theta-\pi/4)/b]^2 \leq 1\}.$$

The vortex is defined by its velocity field (u,v), and its pressure and density fields are constant. For simplicity, the expression of the velocity field is formulated through the stream function ϕ such that $u = -\partial\phi/\partial y$, $v = \partial\phi/\partial x$. The definition of the stream function is different inside and outside the core of the vortex:

$$\phi = \begin{cases} \frac{\Omega}{2}\frac{b(r\cos(\zeta-\theta-\pi/4))^2 + a(r\sin(\zeta-\theta-\pi/4))^2}{a+b} & \text{if } (x,y) \in D_\theta \\ \frac{\Omega ab\cos(2(\zeta-\theta-\pi/4))}{4} e^{-2\cosh^{-1}\left(\frac{r}{\sqrt{a^2-b^2}}\right)} + \frac{\Omega ab\cosh^{-1}\left(\frac{r}{\sqrt{a^2-b^2}}\right)}{2} & \text{if } (x,y) \notin D_\theta \end{cases} \quad (1)$$

where (r,ζ) are polar coordinates [7]. This velocity field is continuous but it is not differentiable at the boundary of D_θ. The maximal velocity of the vortex is reached at the boundary of D_θ and given by $U_v = M_v c_0 = ab\Omega/(a+b)$, with M_v the vortex Mach number associated with the velocity U_v and c_0 the speed of sound. In Sec. 5, the vortex is convected by a horizontal uniform base flow with a velocity $U_c = M_c c_0$, where M_c is the convection Mach number. The velocity field is thus the sum of the convection velocity and the vortex velocity with a center position evolving in time due to the convection.

3. NUMERICAL PARAMETERS

The test case considered consists in a monopole whose radiation is scattered by an elliptic vortex. The positions of the vortex and the monopole within the physical part of the computational domain are represented in Fig. 1. The vortex is centered on $(0,0)$. The monopole is introduced through source terms on the right hand side of the Linearized Euler Equations (LEE) written with the Goldstein pressure π' [8] .

$$\begin{cases} s_{\rho'}(x,y) & = \rho_0 \sin(\omega_0 t) e^{-\frac{(x-x_c)^2+(y-y_c)^2}{b_m^2}}, \\ s_{(\rho u)'}(x,y) & = s_{\rho'}(x,y) u_0(x,y), \\ s_{(\rho v)'}(x,y) & = s_{\rho'}(x,y) v_0(x,y), \\ s_{\pi'}(x,y) & = \frac{\pi_0(x,y)}{\rho_0(x,y)} s_{\rho'}(x,y). \end{cases} \quad (2)$$

The monopole is located at $(x_c, y_c) = (0, -25r_0)$ and radiates at angular frequency ω_0. The wavelength of the acoustic wave is $\lambda_0 = 2\pi c_0/\omega_0$. The Gaussian half-width b_m is $r_0/10$. The results are obtained using a research code developed at Siemens, which resolves the LEE using the Nodal Discontinuous Galerkin Method [9] with polynomial order $N = 4$, and the 6-stage, optimized, low-storage Runge-Kutta scheme from [10]. This code has been previously validated by Williamschen [11]. A triangular unstructured mesh is used. The physical domain extends over $-25r_0 \leq x \leq 25r_0$ and $-35r_0 \leq y \leq 25r_0$, and the buffer zone surrounding it is $5r_0$ wide. The average length of the side of the elements in the physical domain is h. Its value is chosen to ensure at least 10 nodes per λ_0 and r_0, knowing that the distance between nodes is $\Delta = h/4$ for a polynomial order $N = 4$. The ratio λ_0/r_0 varies between $1/4$ and 4. In order not to modify the mesh every time the value λ_0/r_0 changes, only three meshes are considered, with $\Delta = r_0/40$, $r_0/20$ and $r_0/10$. The coarsest mesh satis-

fying the criteria mentioned above is then used depending on the value of λ_0/r_0. The time step Δt is chosen so that $CFL = \Delta t \max_e\{\vec{u}_{e,max}/(\Delta_{norm} R_e)\} \simeq 0.9$, where $\vec{u}_{e,max}$ is the maximal phase speed, Δ_{norm} is the smallest distance between nodes of a normalized element of side $h_{norm} = 1$, and R_e is the radius of the inscribed circle in the element e. The element size at the outer boundary of the buffer zone is $2h$. This stretching of the elements is combined with a dissipative filtering procedure whose amplitude varies between the inner and outer boundaries of the buffer zone. A high-order filter is also applied everywhere in the domain with a cut–off order $N_c = N - 1$. This means that the terms of degree N are cancelled at each time step. A circular array of microphones is placed at a distance of $10r_0$ from the center of the vortex, as shown in Fig. 1. The angle indicating their position in the array is ψ.

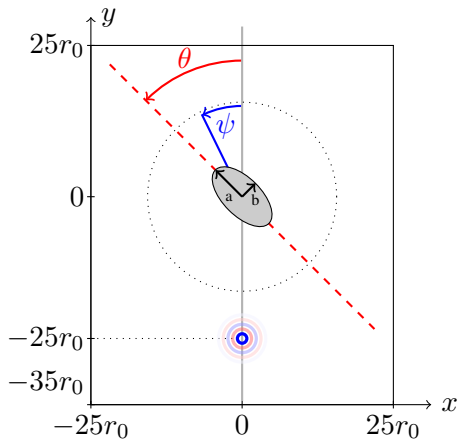

Figure 1: Schematic of the configuration within the physical domain for the static vortex test case.

4. VORTEX AT A FIXED POSITION

In this section, the vortex is not convected and remains centered at $(0, 0)$. Thus, no spectral broadening is observed and only the spatial scattering of acoustic waves is considered, for each of the parameters of interest.

4.1 Influence of the aspect ratio a/b

The effects of the ratio a/b on the spatial scattering of sound are investigated for values ranging from 1, for which the vortex is round, to 5. The other parameters such as the vortex Mach number $M_v = 0.15$ and $\lambda_0/r_0 = 1$ are fixed. The angle θ is set to $\pi/4$. This choice is justified in Sec. 4.2. Instantaneous pressure fields are presented in Fig. 2 for values of $a/b = 1, 2, 3$ and 5. On these fields, constructive and destructive interference beams are visible, due to the scattering of the vortex. A larger number of beams is visible on the left of the vortex ($\psi > 0°$). The beams closer to $\psi = 0°$ seem wider and more intense than the ones visible at larger values of ψ. The number of beams seems to increase with the ratio a/b. The beams that are visible for all four values of a/b seem to remain at the same angular position. The sound scattering is

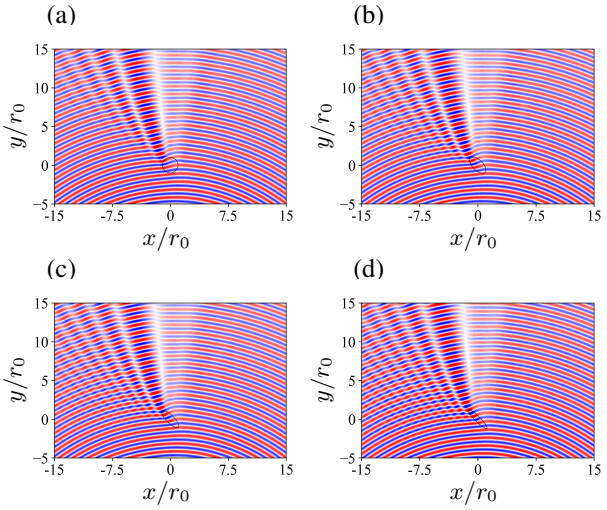

Figure 2: Total pressure fields p' obtained for (a) $a/b = 1$, (b) $a/b = 2$, (c) $a/b = 3$ and (d) $a/b = 5$.

now quantified by the normalized difference between the root-mean-square pressure obtained with and without the vortex $|p'_{rms} - p'_{ref,rms}|/p'_{ref,rms}$ measured over the microphone array. This quantity is represented in Fig. 3 as a function of the ratio a/b and the angle ψ. This cartography confirms the observations made previously. Interference beams are visible mostly for $\psi > 0°$, are wider and more intense close to $\psi = 0°$ than further away. Additional beams appear progressively further and further away from $\psi = 0°$ when the value of a/b increases. The angular position of the interference beams does not evolve with a/b, but the amplitude of the beams increases slightly with a/b.

4.2 Influence of the vortex orientation θ

The effects of the vortex orientation θ on the scattering of sound are discussed. All the vortices considered in

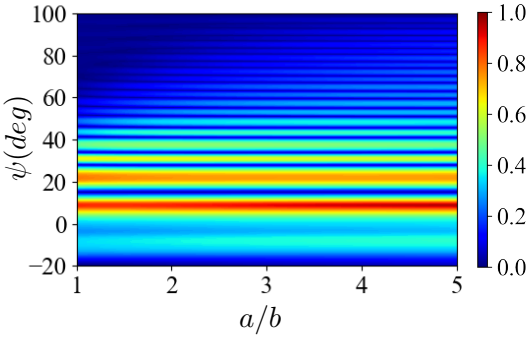

Figure 3: Variations of $|p'_{rms} - p'_{ref,rms}|/p'_{ref,rms}$ as a function of a/b and ψ.

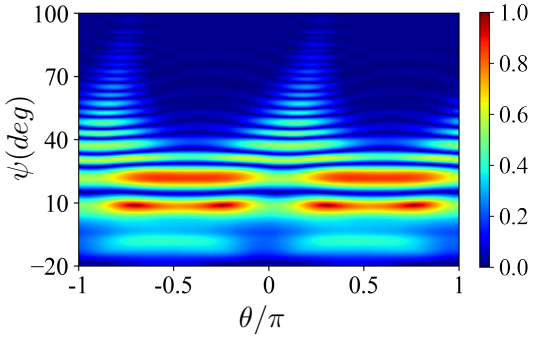

Figure 4: Variations of $|p'_{rms} - p'_{ref,rms}|/p'_{ref,rms}$ as a function of θ and ψ.

this section have a vortex Mach number $M_v = 0.15$ and $\lambda_0/r_0 = 1$. The vortex aspect ratio $a/b = 3$ is chosen. Simulations are performed for $-\pi \leq \theta \leq \pi$. The levels $|p'_{rms} - p'_{ref,rms}|/p'_{ref,rms}$ are displayed in Fig. 4 as a function of θ and ψ. Because of the symmetry of the problem, the interference patterns have a π-periodicity with θ. As for the previous section, the angular positions and the width of the interference beams do not evolve much with θ. The two main interference beams are located around $\psi = 10°$ and $\psi = 20°$. Their amplitudes vary with θ, with the first one having maxima for $\theta = \pm\pi/4$ as well as $\theta = \pm 3\pi/4$ and minima for $\theta = 0$ as well as $\theta = \pm\pi$. The second beam also shows low amplitudes around $\theta = 0$ and $\theta = \pm\pi$. A series of narrow beams with low amplitudes is visible for $\psi > 40°$, but only for values of θ roughly between 0 and $\pi/4$ with a π-periodicity. The choice of $\theta = \pi/4$ in the previous section was thus done because there is both a large number of interference beams over a wide range of angular positions, and the main beams have a large amplitude for this value of θ.

4.3 Influence of the vortex Mach number M_v

The effects of the vortex Mach number M_v are studied in this section. A round vortex and an elliptic one with $a/b = 3$ are considered, their orientation is $\theta = \pi/4$ and the ratio $\lambda_0/r_0 = 1$. To describe the evolution of the interference pattern with M_v, simulations have been performed for values of M_v between 0 and 0.5. The results are plotted in Fig. 5 as a function of M_v and ψ. The interference beams appear under the form of lobes that exist within a limited range of values of M_v. The two cases of $a/b = 1$ and $a/b = 3$ show similar patterns for the interference beams. As M_v increases, narrow beams appear progressively further and farther away from $\psi = 0°$, up to $\psi = 120°$ within the range of M_v considered. The amplitude of the beams is smaller as they appear further away from $\psi = 0°$. The four lobes located around $\psi = 0°$ present the larger amplitudes are and tilted towards higher values of ψ when M_v increases, but the overall position of these lobes appear to shift slightly towards negative values of ψ when M_v increases. The main difference between the two figures is that for any given value of M_v, the beams are spread over a larger angular range for $\psi > 0°$ when $a/b = 3$, and also the amplitudes of the narrow beams far from $\psi = 0°$ are smaller compared to the case $a/b = 1$. Overall, increasing M_v leads to an increase of the scattering angular range.

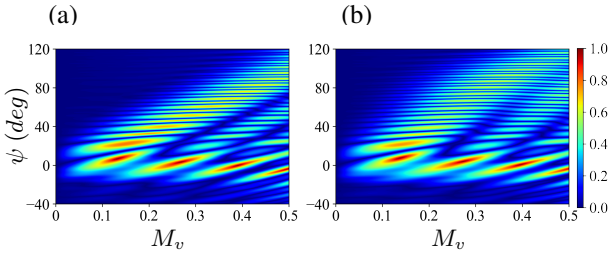

Figure 5: Variations of $|p'_{rms} - p'_{ref,rms}|/p'_{ref,rms}$ as a function of M_v for (a) $a/b = 1$ and (b) $a/b = 3$.

4.4 Influence of the acoustic wavelength λ_0

Finally, the effects of the ratio between the acoustic wavelength and the size of the vortex are studied. The

size of the vortex is fixed, and the frequency of the source varies so that the ratio λ_0/r_0 ranges between $1/4$ and 4. The aspect ratio of the vortices considered are $a/b = 1$ and $a/b = 3$, their Mach number is $M_v = 0.15$ and their orientation is $\theta = \pi/4$. Cartographies of $|p'_{rms} - p'_{ref,rms}|/p'_{ref,rms}$ are plotted in Fig. 6 as a function of λ_0/r_0 and ψ. The two cases considered display a similar distribution of interference beams, and here again, the main difference appears to be in the angular spread of the scattered field, which is larger for $a/b = 3$. For $\psi > 10°$, the lobes are bent upwards. This implies that the interference beams are shifted to greater angles ψ when the wavelength increases. For $\psi < 10°$ the lobes are bent downward, so the beams are shifted to lower angles ψ when λ_0 increases. In general, the lobes seem to widen with λ_0 and their amplitude decreases. For small values of λ_0, the scattered field consists of a large number of narrow but intense interference beams. For large values of λ_0, the interference beams are much less intense and only a few wide beams are visible. This trend is consistent with existing work [12]. Note that, as λ_0 increases and becomes large compared to the vortex (for example when $\lambda_0 \geq 2r_0$), the shape of the vortex does not seem to have much influence on the scattered field [13].

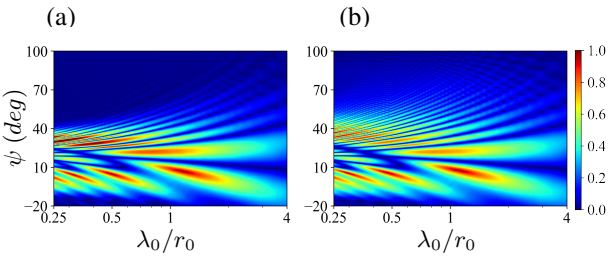

Figure 6: Variations of $|p'_{rms} - p'_{ref,rms}|/p'_{ref,rms}$ as a function of λ_0/r_0 for (a) $a/b = 1$, (b) $a/b = 3$.

5. VORTEX CONVECTED BY A UNIFORM FLOW

In this section, a vortex convected by a uniform flow is considered. The meshes previously used are extended horizontally, such that $-75r_0 \leq x \leq 75r_0$ for the physical domain, allowing the vortex to be convected over a large distance. Only the convection Mach number M_c and the aspect ratio of the vortex vary in this section. The vortex convected along $y = 0$ and its orientation is such that the major axis is parallel to the convection direction. The source emits at a frequency such that $\lambda_0/r_0 = 1$ and the vortex Mach number is $M_v = 0.15$.

5.1 Spatial scattering

The pressure fields obtained when a vortex with $a/b = 3$ is located at $x/r_0 = -30$, 0 and -30 are presented in Fig. 7. The convection effect of the uniform flow on the acoustic waves is clearly visible, with shorter wavelength upstream than downstream of the source, and higher amplitudes upstream. The interference patterns associated with the scattering by the vortex evolve with the position of the vortex. As the vortex convects throughout the domain, the interference patterns rotate clockwise with the orientation of the incident wavefronts radiated by the monopole. The number, width and angular range of the interference beams also change with the position of the vortex. These changes can also be related to the differences in the incident acoustic field in terms of the orientation of the wavefronts (as discussed in Sec. 4.2) and of the wavelength (as discussed in Sec. 4.4). The angle θ varies from $\theta \simeq 0$ when the vortex is far upstream to $\theta \simeq \pi$ when it is far downstream. At the same time, the wavelength varies from $\lambda \simeq \lambda_0(1-M_c)$ far upstream to $\lambda \simeq \lambda_0(1+M_c)$ far downstream. In Fig. 7a, this results in the appearance of a large number of narrow interference beams over a wide angular range. The number of beams appears to decrease progressively in Figs. 7b and 7c, but a wide and intense constructive interference beam appears. The effects of the

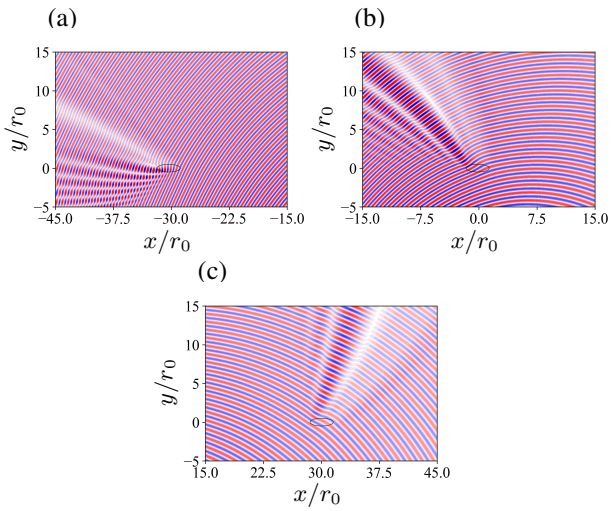

Figure 7: Pressure fields p' obtained for Mach number $M_c = 0.3$ when the vortex is located at (a) $x/r_0 = -30$, (b) $x = 0$ and (c) $x/r_0 = 30$.

Mach number M_c are investigated by considering Mach numbers values $M_c = 0$, 0.3 and 0.6. In absence of convective flow, i.e. $M_c = 0$, the vortex is steady and centered on $(0, 0)$, where the incident wavefronts are tangent to the horizontal direction. When $M_c \neq 0$, the tangent point is located at $t(M_c c_0, 0)$ for $t = 25 r_0/c_0$. The resulting pressure fields are displayed in Figs. 8a, 8b and 8c respectively, when the vortex is located at $(25 r_0 M_c, 0)$. When M_c increases, the interference beams appear to be more curved because the scattering visible in the top left of the figures was generated by the vortex at a position that is more upstream. Some changes related to the effects of the convection on the incident field can be observed in the interference patterns between $M_c = 0.3$ and $M_c = 0.6$, such as a larger number of narrow beams at angles far from the incident waves propagation direction.

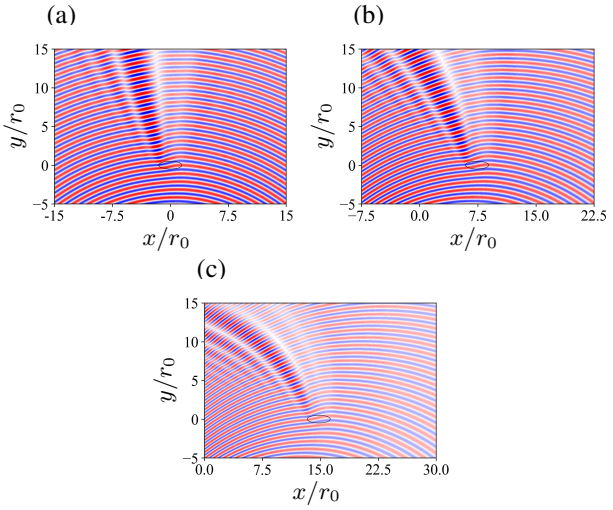

Figure 8: Pressure fields p' obtained for a vortex convected at Mach number (a) $M_c = 0$, (b) $M_c = 0.3$ and (c) $M_c = 0.6$.

5.2 Spectral broadening

5.2.1 Time signals

The pressure field scattered by the convected vortices is first analyzed by looking at the time signals recorded at two observer positions. These signals are plotted as a function of the reduced time t/t_{M_c} where t_{M_c} is defined such that the vortex travels through the physical domain at a velocity $M_c c_0$ during a time $2t_{M_c}$. Thus, the vortex enters the physical domain at $t/t_{M_c} = -1$ and exists at $t/t_{M_c} = 1$. In Fig. 9, the signals received at $x/r_0 = -30$, $y/r_0 = 16$ are plotted for a vortex convected at Mach number $M_c = 0.3$ and at $M_c = 0.6$. Since the signals are plotted as a function of t/t_{M_c}, the period corresponding to the monopole source frequency appears twice as long for $M_c = 0.6$ than for $M_c = 0.3$. On the signals, modulations of the amplitude are visible, that correspond to the interference beams passing over the microphone position. On figure Fig. 9a, those modulations occur between $-0.2 \leq t/t_{M_c} \leq 0.2$ and can be related roughly to the pressure field displayed in Fig. 7a where a wide destructive interference beam appears first, followed by a series of narrower constructive and destructive interferences. In figure Fig. 9b, the modulation pattern is relatively similar but appears later in terms of t/t_{M_c} since the interference beams are lagging further behind the vortex for $M_c = 0.6$ than for $M_c = 0.3$, as shown in Fig. 8. Signals recorded

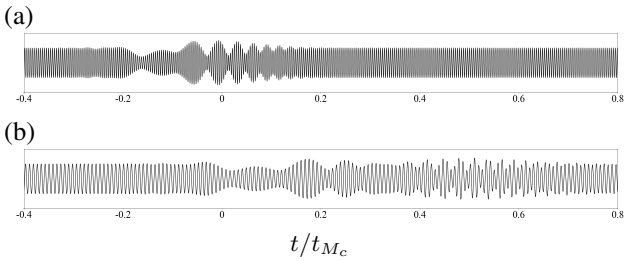

Figure 9: Pressure signal captured upstream at $x/r_0 = -30$, $y/r_0 = 16$ for a vortex convected at Mach number (a) $M_c = 0.3$, (b) $M_c = 0.6$.

downstream of the source at $x/r_0 = 30$, $y/r_0 = 16$ are plotted in Fig. 10 for $M_c = 0.3$ and $M_c = 0.6$. Here, the amplitude modulations are visible over a shorter time extension than for the observer located upstream, and the number of modulations is lower. This can again be related to the pressure field displayed in Fig. 7c where a smaller number of interference beams are visible, and these beams are spanning a smaller angular range. As in Fig. 9, the modulations are shifted in time for $M_c = 0.6$ compared to $M_c = 0.3$, but to a lower extent. These amplitude modulations are expected to have an effect on the spectral content of these signals. As discussed in previous work [12], the vortex is in motion relative to the source and the observer, which suggests Doppler effects leading to frequency modulation of the signals in addition to amplitude modulation. This frequency modulation might not be easily observable on the time signals.

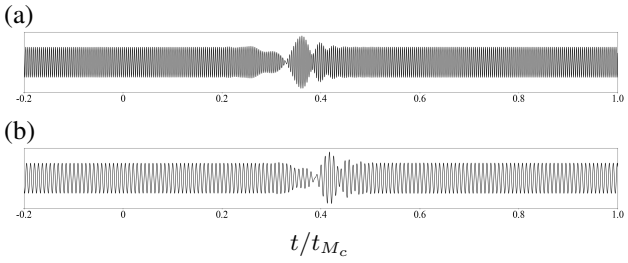

Figure 10: Pressure signal captured downstream at $x/r_0 = 30$, $y/r_0 = 16$ for a vortex convected at Mach number (a) $M_c = 0.3$, (b) $M_c = 0.6$.

5.2.2 *Spectral densities*

Power Spectral Densities (PSD) of the signals previously discussed have been calculated using pressure signals recorded between $-1 \leq t/t_{M_c} \leq 1$ for observers located at $y/r_0 = 16$ and $x/r_0 = -30, 0$ and 30. In Fig. 11, the PSD are plotted as a function of the reduced frequency $(f - f_0)/M_c$ for vortices with aspect ratio $a/b = 1$ and $a/b = 3$ convected by a uniform flow at $M_c = 0.3$. The PSD present a central peak at $f = f_0$, and sidelobes on both sides. A wide lobe is observed for $f < f_0$, while multiple but narrower lobes are observed for $f > f_0$. Overall, the PSD show similar trends for $a/b = 1$ and $a/b = 3$. The main difference is that the sidelobes appear to be wider for $a/b = 1$. When the observation point is moved from upstream to downstream of the source, the sideband visible for $f < f_0$ gets closer to $f = f_0$ and is even merging with the peak. The opposite observation can be made for the sidelobes at $f > f_0$, as they are shifting away from the peak when the observer is moving downstream. The PSD obtained with a convection Mach number $M_c = 0.6$ are presented in Fig. 12. Similar observations can be made overall, with the main difference being the presence of a second lobe at $f < f_0$ for the observer located upstream. Note that, in [12] when the incident acoustic field was a plane wave propagating in a direction normal to the convection flow, increasing M_c led to an increase of the Doppler shift of the scattered field. In that case, the position of the sidelobes plotted as a function of $(f - f_0)/M_c$ is independent of M_c. If the incident field is radiated by a monopole, then the convection affects the incident field as it changes the wavelength and orientation of the wavefronts, but it can also induce convective amplification on the scattered field. Thus, differences may be observed when comparing the PSD plotted as a function of $(f - f_0)/M_c$ at the same observation position but for different M_c. This is the case here when comparing the PSD at $x/r_0 = -30$ and $x/r_0 = 0$ for $M_c = 0.3$ and $M_c = 0.6$, where the positions of the sidelobes differ significantly and a second sidelobe is even visible for $x/r_0 = -30$ at $M_c = 0.6$. For the observer located downstream, the PSD are very similar for $M_c = 0.3$ and $M_c = 0.6$.

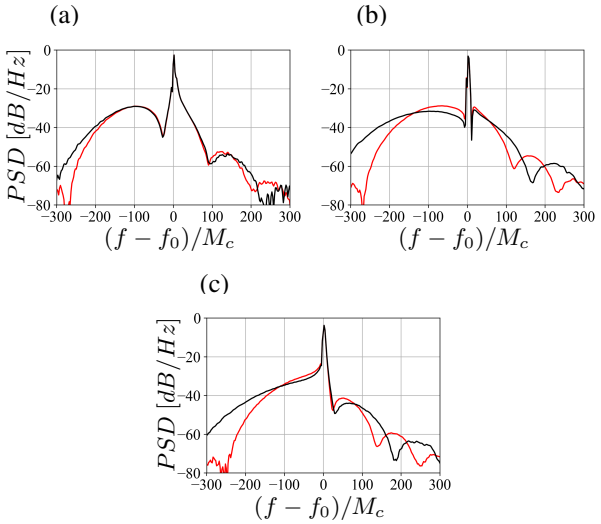

Figure 11: PSD levels obtained at (a) $x/r_0 = -30$, (b) $x/r_0 = 0$ and (c) $x/r_0 = 30$, $y/r_0 = 16$ for $M_c = 0.3$ and — $a/b = 1$ and — $a/b = 3$.

6. CONCLUSION

This work assesses the scattering of acoustic waves by elliptic vortices. It aimed at understanding the effects of the parameters defining the vortex such as its aspect ratio, its orientation with regards to the incident wavefronts, its velocity magnitude and its size relative to the incident acoustic wavelength. Each of the parameters was investigated separately for a stationary vortex scattering the acoustic field radiated by a monopole. The vortex aspect ratio appears to have a relatively mild effect on the scattered field as its increase leads mostly to the appearance of additional, low amplitude interference beams at large scattering angles. The vortex orientation and its velocity magnitude have an influence on the amplitude of interference beams and on the angular range within which interferences are visible. The wavelength to vortex size ratio also affects these characteristics, as well as the angular position and width of the interference beams. The sec-

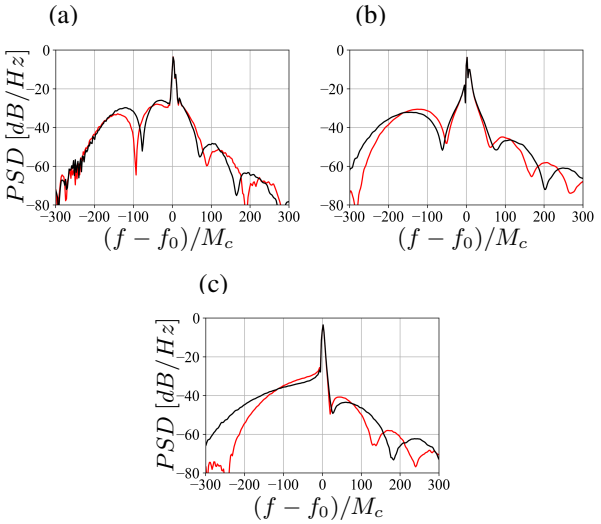

Figure 12: PSD levels obtained at (a) $x/r_0 = -30$, (b) $x/r_0 = 0$ and (c) $x/r_0 = 30$, $y/r_0 = 16$ for $M_c = 0.6$ and — $a/b = 1$ and — $a/b = 3$.

ond part of the paper focuses on the scattering of acoustic waves when the vortex is convected by a uniform mean flow. Since the acoustic source is a monopole, the uniform convection also has a effect on the incident field and modifies the incident wavelength and wavefront orientation depending on the position of the vortex. As a result, changes in the scattering field associated with several parameters in the first part of the paper are combined together when the vortex is convected from upstream to downstream of the source. For an observer at a fixed location, the interferences due to the scattering by the vortex appears as amplitude modulations and frequency modulations associated with a Doppler shift. This leads to a broadening of the spectral content, with the appearance of sidelobes which characteristics such as amplitudes, positions and widths are influenced by the parameters defining the vortex and by the convection velocity.

7. ACKNOWLEDGMENTS

This work is funded by Siemens Digital Industries Software through the PhD program CIFRE 2021/0106. It was granted access to the HPC resources of PMCS2I (Pôle de Modélisation et de Calcul en Sciences de l'Ingénieur de l'Information) of École Centrale de Lyon. The authors would like to acknowledge S. Le Bras for her close and careful supervision of this work.

8. REFERENCES

[1] S. Candel, A. Julienne, and A. Guedel, "Refraction and scattering of sound in an open wind tunnel flow," in *6th ICIASF*, pp. 288–300, IEEE, 1975.

[2] I. Bennaceur, D. C. Mincu, I. Mary, M. Terracol, L. Larchevêque, and P. Dupont, "Numerical simulation of acoustic scattering by a plane turbulent shear layer: Spectral broadening study," *Comput. Fluids*, vol. 138, pp. 83–98, 2016.

[3] R. Ewert, "RPM - the fast random particle-mesh method to realize unsteady turbulent sound sources and velocity fields for CAA applications.," AIAA Paper 2007-3506, 2007.

[4] T. Suzuki, "Coherent noise sources of a subsonic round jet investigated using hydrodynamic and acoustic phased-microphone arrays," *J. Fluid Mech.*, vol. 730, pp. 659–698, 2013.

[5] D. W. Moore and P. G. Saffman, "The density of organized vortices in a turbulent mixing layer," *J. Fluid Mech.*, vol. 69, pp. 465–473, 1975.

[6] H. Lamb, *Hydrodynamics*. Cambridge University Press, 1932.

[7] S. Barré, C. Bogey, and C. Bailly, "Direct simulation of isolated elliptic vortices and of their radiated noise," *Theor. Comput. Fluid Dyn.*, vol. 22, pp. 65–82, 2008.

[8] M. E. Goldstein, *Aeroacoustics*. McGraw-Hill, 1976.

[9] J. S. Hesthaven and T. Warburton, *Nodal Discontinuous Galerkin Methods: Algorithms, Analysis, and Applications*. Springer-Verlag, 2008.

[10] C. Bogey and C. Bailly, "A family of low dispersive and low dissipative explicit schemes for flow and noise computations," *J. Comput. Phys.*, vol. 194, pp. 194–214.

[11] M. Williamschen, "Time-domain DGM for turbofan exhaust noise predictions."

[12] V. Clair and G. Gabard, "Spectral broadening of acoustic waves by convected vortices," *J. Fluid Mech.*, vol. 841, pp. 50–80, 2018.

[13] M. J. Lighthill, "On the energy scattered from the interaction of turbulence with sound or shock waves," *Math. Proc. Cambridge Philos.*, vol. 49, no. 3, pp. 531–551, 1953.